Journal of Sol-Gel Science and Technology
https://doi.org/10.1007/s10971-019-05196-9

ORIGINAL PAPER: CHARACTERIZATION METHODS OF SOL-GEL AND HYBRID MATERIALS

Check for updates

Mechanical properties and decohesion of sol–gel coatings on metallic and glass substrates

David Mercier[1,2] · Arnaud Nicolay[3,4,5] · Abdelhamid Boudiba[4] · Xavier Vanden Eynde[1] · Laure Libralesso[1] · Alain Daniel[1] · Marjorie Olivier[3]

Received: 28 August 2019 / Accepted: 19 November 2019

Abstract

The sol–gel coating method is considered to be simple and easy to implement to lead to organic/inorganic hybrid coatings. In addition, the application of thin films by this technique is inexpensive and applicable on large substrates without form restriction. In this context, thin sol–gel coatings based on a mixture of three alkoxysilanes and synthesized in purely aqueous phase with different thicknesses and with the presence or not of ZrO_2 nanoparticles, were applied on metallic and glass substrates. After application and curing, the mechanical properties of sol–gel coatings were characterized by Berkovich nanoindentation with continuous stiffness measurement mode (CSM). The effective elastic moduli as well as the hardness values were estimated for each coating along the indentation depth and as a function of the substrate material and sol–gel characteristics. The effect of a annealing at higher temperature was also studied. Then, the failure modes of sol–gel coatings were investigated using both Berkovich nanoindentation and nanoscratch technique with a 5 µm radius spherical diamond tip. Careful microscopic observations of residual imprints and residual grooves both exhibit chipping in case of thick coating especially on glass substrate and no dramatic failure for thin coating applied on both substrates. It is shown in this work that the mechanical properties of the sol–gel and the mechanical stability of coatings on substrates are influenced dramatically by the presence of nanoparticles and the thermal treatment. Finally, interfacial fracture toughness of sol–gel coatings on substrate was estimated using analytical model from the literature and Ashby map based on experimental results was created using performance indices in order to proceed to sol–gel coating selection.

✉ David Mercier
david.mercier@ansys.com

[1] CRM Group, Liege, Belgium

[2] Ansys, Inc.—Granta Education Team, Lyon, France

[3] University of Mons, Faculty of Engineering, Mons, Belgium

[4] Materia Nova, Mons, Belgium

[5] Ionics Group, Mons, Belgium

Published online: 03 December 2019

Graphical Abstract

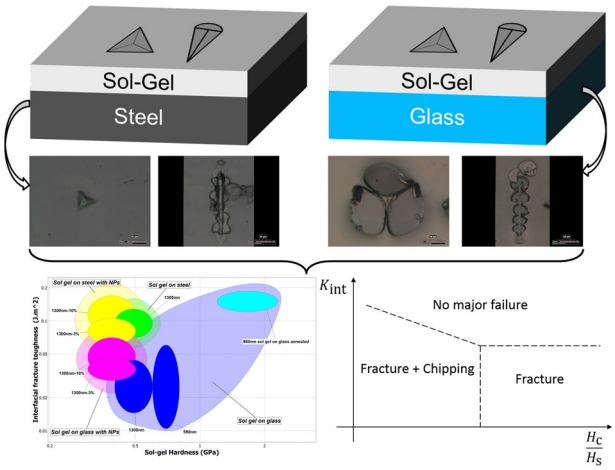

Highlights

- Mechanical characterization of sol–gel coatings using a combination of different nanomechanical experiments.
- Effects of nanoparticles addition and thermal treatment on mechanical coating stability.
- Construction of Ashby map using experimental results for sol–gel coating selection.

Keywords Organic/inorganic hybrid coatings · Nanoindentation · Nanoscratch · Failure mode · Interfacial fracture toughness · Selection map

1 Introduction

The protection of metals and common alloys like stainless steel [1, 2], aluminum alloys [3, 4], or magnesium alloys [5] against corrosion, wear and scratches is an important task. For that purpose, ceramic based coatings are investigated and used by means of diverse methods, e.g., physical vapor deposition and plasma enhanced chemical vapor deposition [6, 7]. But these approaches require expensive equipments and it is often difficult to obtain a good coverage for a complex form of substrat. Another way to enhance the anticorrosion [1, 8–10] and surface mechanical properties [11–16] is to use sol–gel methodologies. Indeed, since the 90s, numerous publications have been published on the protection of metallic substrates by sol–gel layers. The interest with regard to sol–gel technology comes from the simplicity of implementation but also the fact that there is a chemical bond of the coating with the metallic surface [17]. Furthermore, another major advantage of the sol–gel route is the possibility to provide a protection to the metal against corrosion from nontoxic precursors and without adding of a carcinogenic compound such as hexavalent chromium [18].

The most of the publications presents sol–gel developed in organic solvant: ethanol [9, 19–21], isopropanol [22–24], … with addition of 0–25% by volume of water which is sometimes necessary for a good hydrolysis of precursors. But there are also some water-based sol–gel, for example the case of Vignesh et al. [4] who prepared a mercaptopropyltrimethoxysilane sol–gel for anticorrosive application of aluminum. Capelossi et al. [25] investigated the corrosion protection of the cladded 2024 aluminum alloy, anodized and protected by application of a hybrid sol–gel coating with a high water content (58% v/v). Finally some publications can be found with purely aqueous sol–gel composition. Roussi et al. [26] synthesized an aqueous sol–gel by dropwise addition of GPTMS and TEOS in deionized water, while Fedel et al. [27] studied the properties of a aqueous silane pretreatments. This leads to environmentally friendly coating chemistry.

In order to improve or bring some properties at the coatings, various types of additions such as metal oxides: ZnO [28], TiO_2 [29, 30], ZrO_2 [31, 32], or SiO_2 [33] have been incorporated into polymers or sol–gel coatings according to the required properties. Among the available nanoparticles (NPs), ZrO_2 seems to be a good candidate to improve the mechanical properties of coatings thanks to its good chemical stability and its high hardness resulting in good wear resistance. Piwoński et al. [32] showed that ZrO_2 NPs enhanced the tribological performance of alumina layers and Song et al. [34] revealed that PEEK/ZrO_2 composite coatings could improve the tribological properties of Ti6Al4V.

Moreover, mechanical behavior of sol–gel coatings have been extensively studied by nano- and microindentation experiments in the literature (elastoplasticity [35–42], brittle behavior [35, 43–45], and adhesion [45–48]). Possible fracture events can occur in thin films and coatings during

indentation and scratch experiments, like radial crackings, spallation, or delamination [49]. From the observations of chip formation beside an indent or in front of a scratch, analytical models from Thouless [50], Den Toonder et al. [45], Malzbender and De With [51], Xie and Hawthorne [52], Bull and Berasetegui [53] can be used to estimate the fracture energy of the coating.

In this paper, the preparation of purely aqueous sol–gel coatings and the mechanical properties at the nanoscale are detailed. The alkoxysilane solutions consist of a mix of three different precursors: tetraethoxysilane (TEOS), methyltriethoxysilane (MTES), and glycidyloxypropyltrimethoxysilane (GPTMS). The inorganic part have to provide the hardness, while the organic chains have the advantage of enhancing flexibility to avoid cracks in the coatings. In the literature we notice that the mechanical performance of a coated material depends on the intrinsic properties of coating as well as the film thickness and the adhesion of the sol–gel coating to the substrate. Nanoindentation and nanoscratch experiments were performed to study the influence of the sol–gel coating thickness, the thermal treatment, and the nature of the substrate on the layer properties, including elastic modulus, hardness, and adhesion. The influence of ZrO_2 NPs incorporation on this properties is also presented. Finally, sol–gel coating selection is performed following Ashby's methodology, based on performance indices and material properties maps [54, 55].

2 Materials and experimental methodologies

2.1 Materials

The alkoxysilane precursors used were glycidyloxypropyltrimethoxysilane (GPTMS, Sigma-Aldrich, >98% purity), tetraethoxysilane (TEOS, Merck, for synthesis), and methyltriethoxysilane (MTES, Alfa Aesar, 98% purity). These products were used as received without further purification. Commercially available ZrO_2 nanocharges were supplied by IoLiTec, and with an average size around 30–60 nm, and pure at 99.9%. Microscopic observations were performed using a scanning electron microscope (Fig. 1). The substrate material studied was AISI-304 polished stainless steel. Because of its heating limitation (yellowing from 210 °C for 1 min in air), the glass substrate was also used as reference (smooth surface, homogeneous bulk material with isotropic properties, and heat resistant). Before application:

- The stainless steel sheets were degreased with acetone.
- The glass substrates were cleaned with RBS^{TM} detergent and then ethanol.

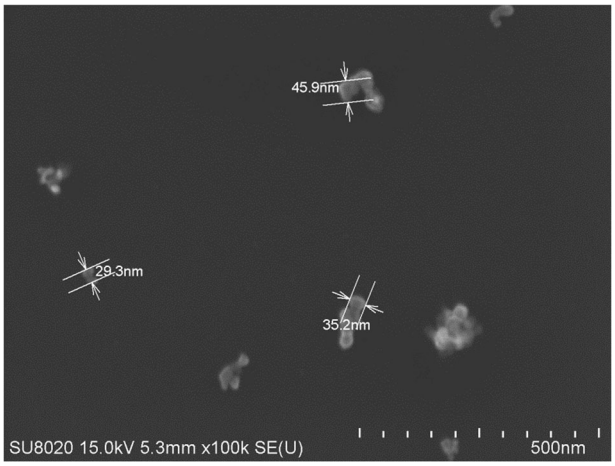

Fig. 1 SEM micrograph of zirconia nanopowder

Table 1 Summary of the different matrices used for sol–gel coatings deposition

Matrix	#1	#2	#3	#4
Dry extract (wt%)	4.4	9.9	12.7	14.7
Thickness (nm)	275	590	960	1300

2.2 Sol–gel coating elaboration, application, and morphology

Four matrices have been prepared with a different overall percentage of precursors. The ratio between the three precursors remains equal and the hydrolysis was catalyzed with acid. The modification in the precursors concentration was carried out to modify the dry extract of the matrix and thus the deposited layer thickness. Table 1 summarizes these different matrices. The films were applied on both substrates at room temperature by dip coating. The sol–gel network is obtained for each sample by drying and curing at 180 °C for 1 h. Homogeneous, transparent, colorless, and barrier coatings were obtained. The coating thickness was measured by Dektak profilometer on glass (Table 1). Two concentrations of ZrO_2 were studied: 3 and 10 wt% compared with the dry extract. A thermal annealing at 670 °C during 3 min was carried out on some glass samples to evaluate the temperature effect on the mechanical properties of the coating. No modification of glass mechanical properties is assumed after this tempering step. For some matrices, zirconia NPs were beforehand dispersed in water using an ultrasonic probe. Surface roughness of sol–gel coatings has been estimated from topographic images obtained by atomic force microscopy (AFM). 5 µm × 5 µm maps were recorded with 512 × 512 data points. AFM measurements were carried out with a Dimension Edge

Table 2 Summary of the roughness values obtained by AFM on different sol–gel coatings

Matrix	#1	#1	#4	#4	#4
Substrate	Glass	Glass	Steel	Glass	Glass
Thickness (nm)	275	275	1300	1300	1300
Thermal treatment	No	Yes	No	No	No
Presence of NPs	No	No	No	No	Yes (10%)
Surface roughness—Sa (nm)	3.1	6.2	0.6	1.4	1.3
Surface roughness—Sq (nm)	4.7	7.9	0.7	1.7	1.9

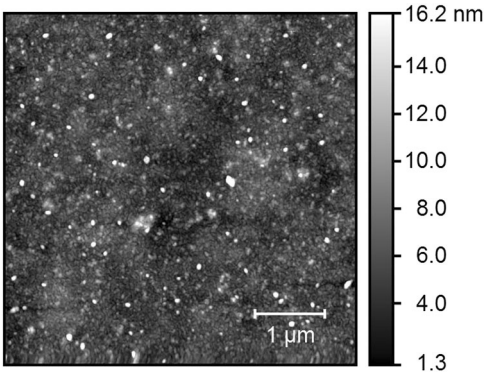

Fig. 2 AFM observation of 1.3 µm sol–gel coating on glass subtrate, with 10% of NPs

from Bruker in tapping mode. Sol–gel coating surfaces are flat and roughness values given Table 2 are kept to a nanometric level whatever the deposition and elaboration steps. There is no clear evidence of thermal annealing effect or addition of NPs, change of the substrate or increase of the sol–gel coating thickness, on the surface roughness. AFM observation shows a homogeneous dispersion of the NPs whatever the percentage (Fig. 2).

2.3 Experimental techniques

The mechanical properties of the sol–gel films and the substrates were studied using the nanoindentation technique with a diamond Berkovich indenter. A Nanoindenter XP™ (MTS Instruments) with a continuous stiffness measurement (CSM) module was used, allowing the continuous measurement of contact stiffness (S), applied load (L), and indentation depth (h). Indentation tests were performed to a maximum depth of 2 µm, and under a constant deformation rate of 0.05 s^{-1}. The area function of the Berkovich indenter was calibrated against fused silica standard. Grids of indents (matrix of 6 × 6) separated by 50 µm were made on each sample in order to obtain average values.

Scratch tests were performed in parallel on each coating/substrate system (ten scratches per sample), using a Nanoindenter XP™ (MTS Instruments), to qualitatively assess the relative resistance of the materials to scratching and the adhesion of the coating to the underlying substrate. A spherical diamond indenter (5 µm tip radius and 90° half angle) was used to perform the scratch tests. The indenter scratched only one time the sample, over a length of 100 µm, with an increasing linearly applied normal load, until a maximum of 100 mN, at a constant velocity of 5 µm s^{-1}.

Optical microscopic (OM) observations of the residual indents and scratch grooves are performed either in situ the nanoindenter with a magnification of ×10, or using a 3D Digital KH-8700 (Hirox company, Japan) microscope equipped with a OL-700 II objective. Micrographs of residual imprints are also aquired by scanning electron microscopy (SEM) using a Hitachi SU8020 and by AFM with a Dimension Edge from Bruker in tapping mode.

2.4 Estimation of sol–gel coating mechanical properties

Both elastic modulus and hardness were determined from the load–displacement curves, following the method given by Oliver and Pharr [56, 57]. The reduced elastic modulus (E') and the hardness (H) for the coating were both calculated according to the following equations:

$$E' = \frac{S}{2\beta_k}\sqrt{\frac{\pi}{A_c}} \quad (1)$$

$$H = \frac{L}{A_c} \quad (2)$$

With β_k equal to 1.034 for a Berkovich indenter, according to King [58], and with A_c the contact area between the indenter and the surface sample. Using reduced modulus values obtained from Eq. 1 and assuming Poisson's ratios (ν) of 0.225, 0.25, and 0.29, respectively, for the different sol–gel coatings (according to Malzbender et al. [47]) the glass (according to Makishima and Mackenzie [59]) and the stainless steel (according to Ledbetter [60]) substrates, it is possible to assess elastic modulus (E) of coatings and reference susbtrates using Eq. 3.

$$E = \left(1 - \nu^2\right)\left(\frac{1}{E'} - \frac{1 - \nu_{\text{ind}}^2}{E_{\text{ind}}}\right)^{-1} \quad (3)$$

With υ_{ind} and E_{ind}, respectively, the Poisson's ratio (equal to 0.07) and the elastic modulus (equal to 1040 GPa) of the diamond indenter [54, 61].

In the case of thin film indentation, the measured mechanical properties are influenced by the substrate. In this paper, mean values of elastic modulus and hardness of sol–gels are extracted at 10% of the coating thickness, according to the Bückle's rule of thumb [61].

Malzbender et al. proposed also to use analytical models to extract the mechanical properties of the sol–gel coatings [42, 47]. For layers thinner than 500 nm, this empirical rule is not valid, since substrate effect occurs and area function is not really well defined for too small indentation depths (<50 nm) given tip defect, surface topography, and the presence of surface contamination… An easy solution is to use an analytical multilayer model to extract elastic modulus of the coating [62, 63]. Finally, average values of the different substrates mechanical properties are calculated for indentation depths between the surface and the maximum indentation displacement (2 µm).

Fracture toughness (K_{Ic})in mode I can be estimated from the critical load (L_c) when radial cracks appear in the coating or the substrate [64, 65]. The determination of toughness is based on Vickers indentation, but this approach is also valid for Berkovich indentation [47] and given by the following equation:

$$K_{Ic} \approx \sqrt[4]{\frac{H^3 L_c}{21.7 \times 10^3}} \tag{4}$$

When fracture and pop-in on a load–displacement curve from indentation tests are correlated, the energetic model from Li et al. [47, 66] can be used to determine coating toughness:

$$K_{Ic} = \left[\left(\frac{E}{(1-\nu^2)2\pi C_R}\right)\left(\frac{U_{pop-in}}{t}\right)\right]^{0.5}, \tag{5}$$

where E is the elastic modulus, ν is the Poisson's ratio of the layer, $2\pi C_R$ is the crack length in the film plane, U_{pop-in} the strain energy difference before and after cracking (roughly the aera below a pop-in), and t is the coating thickness.

2.5 Estimation of work of adhesion

Coating work of adhesion can be assessed from scratch experiments, knowing the critical load (F_c) just before chipping when elastic energy is released by interfacial fracture [66–70]. According to the literature, Malzbender et al. [47] proposed to define the work of adhesion (U) by the following equation:

$$U = \frac{1}{2tE}\left(\frac{\nu\mu F_c}{w}\right)^2 \tag{6}$$

This formulae depends on geometrical parameters (the coating thickness (t) and the width scratch track (w)) and the mechanical properties of the coating (elastic modulus (E) and Poisson's ratio (ν)) and the friction coefficient between the sol–gel coating and the indenter in diamond (μ).

2.6 Estimation of interfacial toughness

Coating interfacial toughness ($K_{c,\mathrm{int}}$) is a combination of the mode I and II fracture toughness and can be estimated, knowing elastic properties of coating/substrate system and using following equations [47, 51]:

$$E_{\mathrm{int}} = \left(\frac{1}{2}\left(\frac{(1-\nu^2)}{E} + \frac{(1-\nu_s^2)}{E_s}\right)\right)^{-1} \tag{7}$$

$$K_{c,\mathrm{int}} = \sqrt{\Gamma E_{\mathrm{int}}} \tag{8}$$

With E_{int} being the reduced interfacial elastic modulus, E_s and υ_s are, respectively, the reduced elastic modulus and the Poisson's ratio of the substrate. Γ is the fracture energy (in J/m²), calculated from indentation and scratch experimental tests with chips geometry and coating properties. A first easy model to get this fracture energy is given by Thouless [50]:

$$\Gamma_{\mathrm{Thouless}} \approx 0.35\frac{Et^5}{l^4}\left(\frac{\tan\beta + \frac{w}{l}}{\tan\beta + \frac{w}{2l}}\right)^2 \tag{9}$$

E and t are, respectively, the elastic modulus and the thickness of the coating, and β, w, and l are geometrical parameters given Fig. 3.

Den Toonder proposed another model [45], based on the model of Thouless [50], taking into account the curvature of the chip and the residual stress in the coating:

$$\Gamma_{\mathrm{Den\ Toonder}} \approx \Gamma_{\mathrm{Thouless}} + \frac{t(1-\upsilon)\sigma_r}{E} + \frac{3.36(1-\upsilon)t^3\sigma_r}{l^2}\left(\frac{\frac{w}{2l} + \frac{\beta\pi}{2}}{\frac{w}{2l} + \beta\pi}\right) \tag{10}$$

E, υ, and t are, respectively, the elastic modulus, the Poisson's ratio, and the thickness of the coating, σ_r the residual stress in the coating and β, w, and l are geometrical parameters given Fig. 4. In fact, Den Toonder replaced $\tan(\beta)$ with $\beta\pi$ in his paper, but this assumption is only valid for small angles, which is not always the case when chipping occurs during scratch tests. This model is also

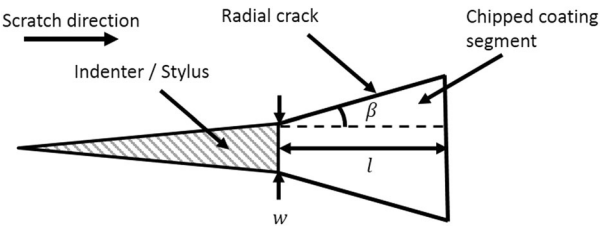

Fig. 3 Scheme of a chip in front of a scratch groove (Thouless [50])

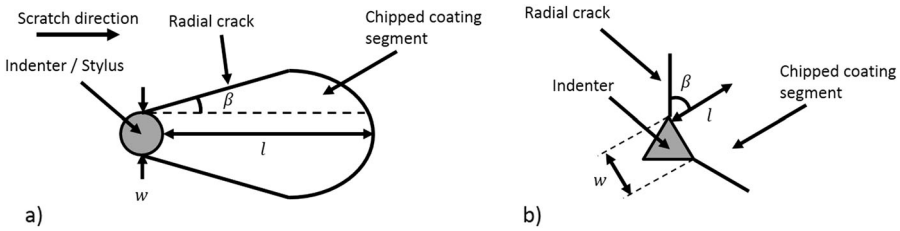

Fig. 4 Schemes of a chip **a** in front of a scratch groove (Den Toonder et al. [45], Malzbender and De With [51]) and **b** beside an indent (Bull and Berasetegui [71])

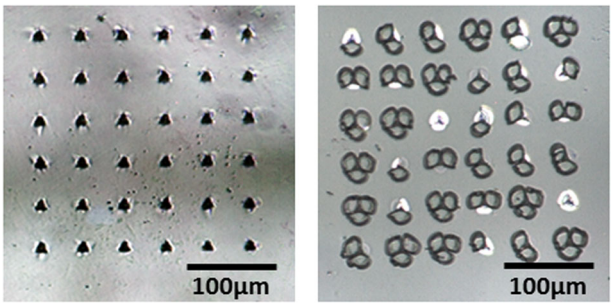

Fig. 5 Optical microscopic observations of the indentation grids performed on the 1.3 µm thick sol–gel coatings on steel (on left) and glass (on right) substrates

valid for chips around residual indents, according to Bull and Berasetegui [71].

3 Results and discussion

3.1 Mechanical properties of sol–gel coatings

From indentation experiments, OM observations of the indentation grids performed on the sol–gel coatings on steel and glass substrates are given Fig. 5. Given that, no network of residual cracks is observed on the different sol–gel coatings (whatever the deposition conditions) (Fig. 5), it is assumed that the residual stress level tends to be very low in the studied sol–gel coatings. The corresponding curves with the evolution of elastic modulus and hardness as a function of indentation displacement normalized by coating thickness are given respectively in Figs 6 and 7. Discontinuities (=slope variations) observed at depth higher than 500 nm on the mechanical properties evolution are attributed to failure mechanisms (cracks or chips formation, decohesion/delamination, fracture in the substrate…). In the case of sol–gel coatings on glass indentation tests, failure modes of spallation and chipping are observed in Fig. 5, with the formation of chips around indents, which induce discontinuities on the load–displacement curves and on the evolution of elastic modulus and hardness. No fracture is observed for indentation on sol–gel coating deposited on steel, given the fact that steel substrate is softer than glass. Regarding Figs 6 and 7, it is obvious that calculated values of mechanical properties increase with indentation depth because of substrate effect. Given all these experimental observations, the average elastic modulus and hardness values for the different coatings are extracted at 10% of the coating thickness before chipping and influence of substrate using Eqs. 1–3, and are given Table 3, with mechanical properties of the different substrates. In this work, no acceptable average value for mechanical properties are extracted for the 275 nm thick sol–gel coating, even using multilayer elastic model considering that elastic modulii ratio for the coating and the substrate is really too high (>10). It sounds that hardness of the sol–gel is closed to 0.5 GPa and elastic modulus is about 5 GPa, whatever the coating thickness or the presence of NPs. The slight difference between sol–gel on glass (higher hardness values) and sol–gel on steel (higher elastic modulus values) is attributed to the substrate effect (steel is stiffer and softer than glass substrate). It is worth to mention that, the 960 nm thick sol–gel on glass with annealing tend to be at least 3 times harder and stiffer. As this difference does not come from substrate properties evolution with annealing, the increase of sol–gel hardness and sol–gel Young's modulus can be attributed to a coating densification thanks to the annealing step, which is in agreement with the literature [72].

3.2 Qantitative analyis of mechanical failure

3.2.1 Difference between steel and glass substrates

In this part, the mechanical failure of the sol–gel coating is discussed as a function of the substrate nature. For that, examples of microscopic observations of residual indents and residual grooves are given Fig. 8. No indentation chip or crack during indentation for sol–gel layer on steel is observed but chipping clearly occurs for sol–gel on glass indentation. In parallel, interfacial decohesion (bulging) of the sol–gel coatings occurs with both substrates before chipping (see white arrow in Fig. 8c, d). A higher stress level is reached during scratch tests compared with indentation experiments, which leads to the chipping failure of the sol–gel coating on steel substrate. It is also easier to qualify breakdown of the sol–gel during scratch. In the case of glass substrate, chips are circular and bigger as soon as load is increased. But with steel substrates, chips are not

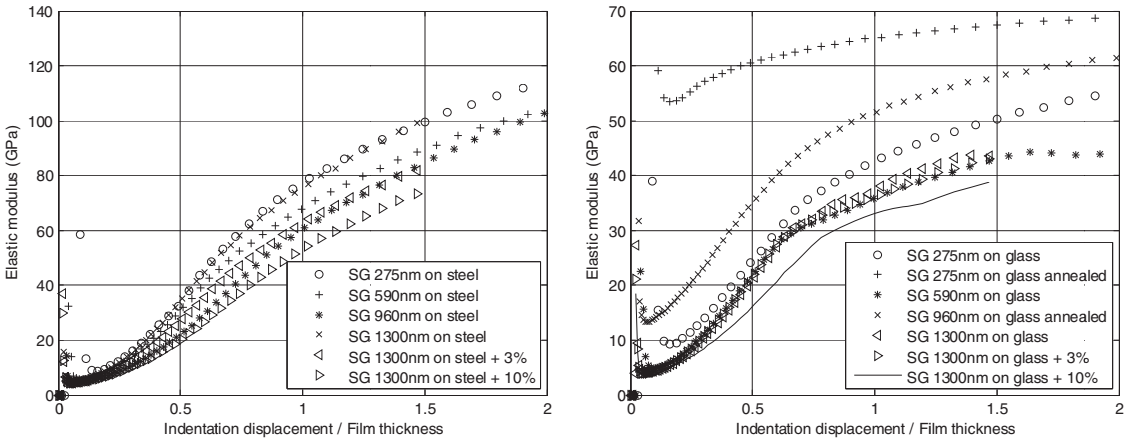

Fig. 6 Evolution of elastic modulus as a function of indentation depth normalized by coating thickness obtained for sol–gel coatings on steel (on the left) and glass substrate (on the right)

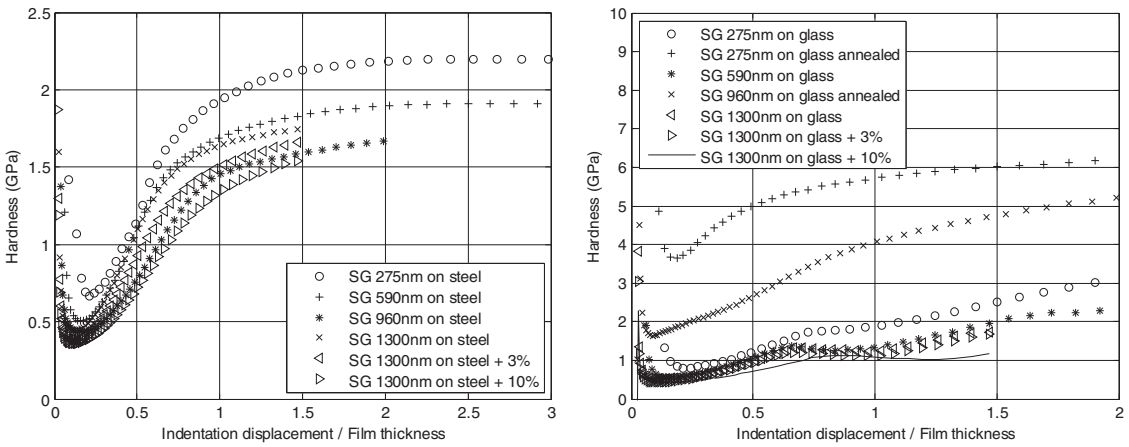

Fig. 7 Evolution of hardness as a function of indentation depth obtained for sol–gel coatings on steel (on the left) and glass substrate (on the right)

Table 3 Summary of mean mechanical properties values of the different sol–gel coatings and the substrates, obtained from nanoindentation experiments

Sample	Thickness of the sol–gel coating (μm)	Thermal treatment (3 min/670 °C)	Presence of nanoparticles	Mean elastic modulus (GPa)	Mean hardness (GPa)	Coating spallation
304 stainless steel	Bulk	No	No	177.7 ± 5.8	3.8 ± 0.8	Ø
Sol–gel coatings on 304 stainless steel substrate	0.28	No	No	Ø	Ø	No
	0.59	No	No	6.2 ± 0.2	0.6 ± 0.1	No
	0.96	No	No	5.5 ± 0.1	0.5 ± 0.1	Yes
	1.3	No	No	5.9 ± 0.4	0.5 ± 0.1	Yes
			3% ZrO_2	5.0 ± 0.2	0.4 ± 0.1	Yes
			10% ZrO_2	4.9 ± 0.1	0.4 ± 0.1	Yes
Glass	Bulk	No	No	71.1 ± 2.0	6.2 ± 0.3	Ø
Sol–gel coatings on glass substrate	0.28	No	No	Ø	Ø	No
		Yes	No	Ø	Ø	No
	0.59	No	No	5.3 ± 0.2	0.7 ± 0.1	Yes
	0.96	Yes	No	14.7 ± 4.2	1.7 ± 0.5	Yes
	1.3	No	No	4.6 ± 0.2	0.5 ± 0.1	Yes
			3% ZrO_2	4.3 ± 0.2	0.4 ± 0.1	Yes
			10% ZrO_2	4.4 ± 0.2	0.4 ± 0.1	Yes

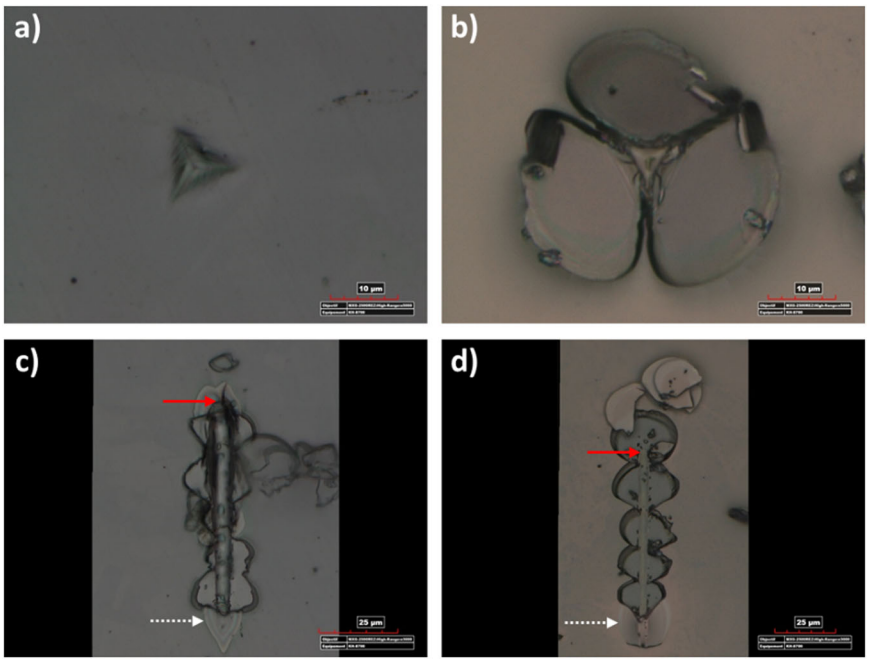

Fig. 8 Examples of residual indents (on the top) and residual grooves (on the bottom) obtained, respectively, by nanoindentation and nanoscratch techniques for the 1.3 µm thick sol–gel coatings without NPs on steel (left) and glass (right) substrates. Red arrows indicate the end of the scratch tests (corresponding to the maximum applied normal load). Black dashed arrows indicate decohesion of the sol–gel coatings

Table 4 Summary of mean work of adhesion values of different sol–gel coatings obtained from scratch experiments

Sample	Sol–gel coating thickness (t) (nm)	Thermal treatment (3 min/670 °C)	Critical load (L_c) (mN)	Track width (w) (µm)	Work of adhesion (U) (J/m²)
Sol–gel coatings on 304 stainless steel substrate	1300	No	30–40	2.8–3.5	18.3 ± 4.3
Sol–gel coatings on glass substrate	275[a]	No	5–8	1.8–2.2	7.6 ± 2.2
	590	No	12–16	2.6–3.3	8.7 ± 1.8
	960	Yes	50–60	2.9–3.4	23.1 ± 3.8
	1300	No	15–25	3–3.6	7.3 ± 2.2

[a]For the calculation, a Young's modulus of about 5.3 GPa is assumed for the 275 nm thick sol–gel

reproducible and asymmetrical, which comes from the median cracks generated in front of the groove (see red arrow in Fig. 8c, d). These experimental results are in agreement with the literature, especially the map of the main scratch test failure modes in terms of substrate and coating hardness [73]. Finally, scratch experiments are quantitatively analyzed, and work of adhesion is estimated using Eq. 6 for different sol–gel coatings. A friction coefficient between diamond tip and sol–gel coating is assumed to be about 0.3 and calculated work of adhesion values are reported in Table 4. In case of samples cured with an optimized thermal treatment and in case of sol–gel on softer substrate than glass, adhesion is promoted and the sol–gel is better complying the deformation implied by the indenter.

3.2.2 Addition of nanoparticles in the sol–gel

The effect of NPs addition into the sol–gel on the coating adhesion to the substrate is discussed in this paragraph. Microscopical observations of experimental 6 × 6 indentation grids for 1.3 µm thick sol–gel with (3 and 10%) and without NPs are given in Fig. 9. Each grid can lead to the formation of $3 \times 36 = 108$ chips, if the failure is total in the sol–gel during indentation tests. Qualitatively, the NPs incorporation seems to promote adhesion of the sol–gel on the substrate, with mainly bulging occurring on the specimen with 10% NPs. But for both samples with 3% and without NPs, about 95% of indents have at least one chip. Based on these observations, the frequency of chips formation is given for the three samples with Fig. 10. Using this histogram, about 2, 1.6, and 0.2 chips/indent are estimated, respectively, for the samples without and with 3 and 10% of NPs.

3.2.3 Analysis of indentation experiments on glass substrate (1.3 µm thick layer)

As multiple adhesive and cohesive failure mechanisms occur during these indentation or scratch experiments, the

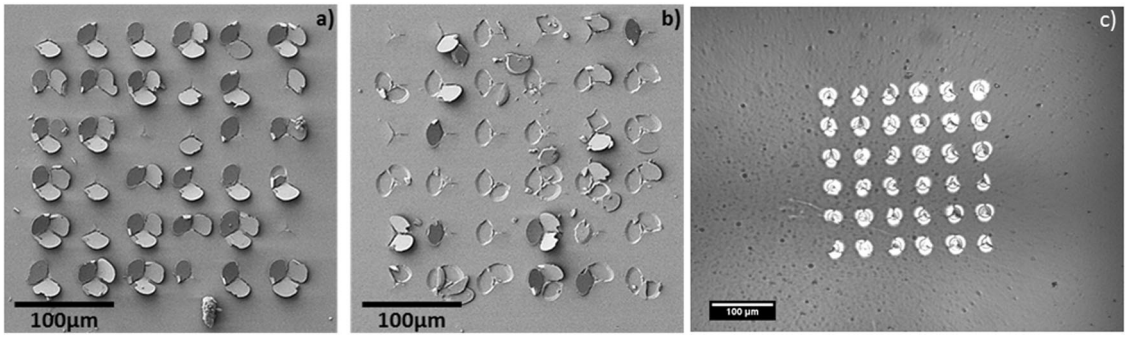

Fig. 9 Microscopical observations of indentation arrays on 1300 nm thick sol–gel coatings on glass substrate: **a** without ZrO_2 nanoparticles (SEM), **b** with 3% (SEM), and **c** 10% of ZrO_2 nanoparticles (OM)

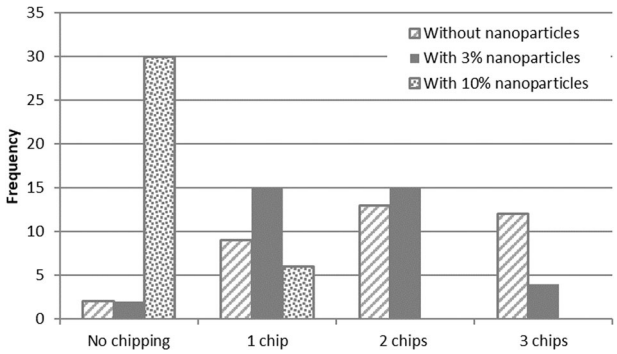

Fig. 10 Distribution of number of chips around indents for sol–gel coating with (3 or 10%) or without NPs

analysis of indentation experiments for sol–gel layer on glass substrate is performed in order to extract a coating fracture toughness. OM view of the nanoindentation grid and detailed SEM or optical observations of indents for the 1.3 µm thick sol–gel with corresponding (dL/dh)-displacement curves of specific indents are given in Fig. 11. (dL/dh)-displacement curves are plotted to emphasize slope variations.

Based on optical observations (Fig. 11i, j), it is obvious that indents #22 and indents #23 have very different residual morphologies. On one hand, no chipping and only radial cracking with bulging effect (irisation phenomenon) is present on indent #22, and on the other hand chipping is clearly visible with indent #23. Nevertheless, the radial cracking occuring for indent #22 might be not confined on the coating, but radial cracking may occur inside the substrate. This first analysis based on optical observations was verified with AFM measurements on indents presenting similar residual morphologies (Fig. 12). These AFM observations show that bulging effect is confirmed in the case of no chip formation (Fig. 12a, a′). This bulging effect is may be due to the compression of the coating during indentation process, which induces buckling and the final bulging of the coating. A residual indent with chipping but no residual chip around the indent is also analyzed (Fig. 12b, b′), and the chip thickness sounds to be close to the sol–gel coating thickness (about 1–1.3 µm). This result would imply that bulging effect is mainly due to interfacial decohesion between the coating and the substrate.

Other indents #7, #4, #25, and #6 are analyzed (Fig. 11b–j) and present respectively no chip, one chip, two chips, and three chips. From corresponding nanoindentation (dL/dh)-displacement curves, it sounds that multiple negative peaks can be observed. These negative peaks are usually attributed during indentation tests to energy dissipation phenomenon (e.g., plasticity, fracture, decohesion, or phase transformation…). Two first negative peaks always seen below 1.5 µm indentation depth, which is roughly the coating thickness, are attributed to radial fracture in the coating and interface decohesion. And other negative peaks above this limit tend to correspond to the number of chips formed around the indent. Some authors proposed to use some criteria for peak detection (e.g., dL/dh^2 vs. h^2 or L/h^2 vs. h^2) to lead to critical loads estimation for each chipping step [65]. Based on our analysis and the literature, a scenario for the failure mechanisms evolution in the sol–gel coating during indentation is proposed (Fig. 13). It is clear that the proposed (dL/dh) vs. displacement curve is enough in this case to emphasize slope variations and the proposed chronological scenario for the sol–gel failure is:

(1) Radial craking.
(2) Delamination or interfacial decohesion.
(3) Successive (or simultaneous) chipping (up to three chips).

Based on this analysis, critical loads can be statistically extracted for each failure event, from indentation load–displacement curves. The determination of the first critical load corresponding to the radial cracking allows fracture toughness estimation using Eq. 4 and values for material properties given Table 3. For the 1.3 µm thick

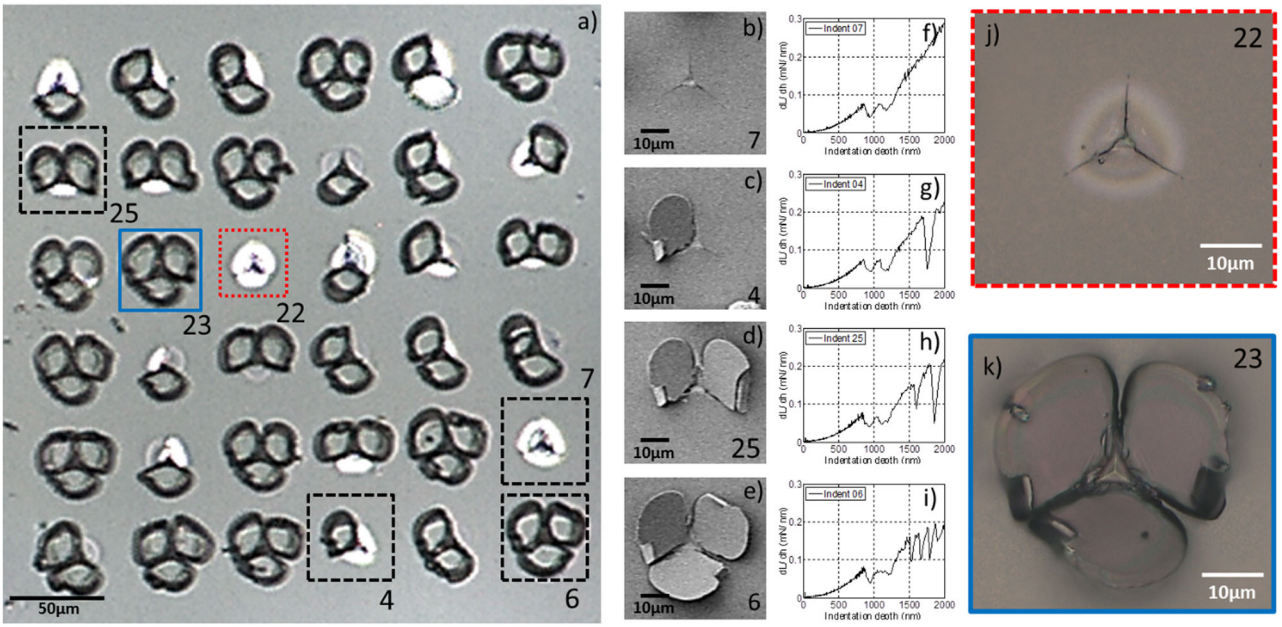

Fig. 11 **a** Optical microscopic view of the nanoindentation grid and SEM observations for the 1.3 µm thick sol–gel with corresponding (dL/dh)-displacement curves of specific indents with **b** and **f** no chipping, **c** and **g** formation of one chip, **d** and **h** formation of two chips, and **e** and **i** formation of three chips. **j**, **k** Are respectively detailed optical microscopic observations of indents without or with chipping

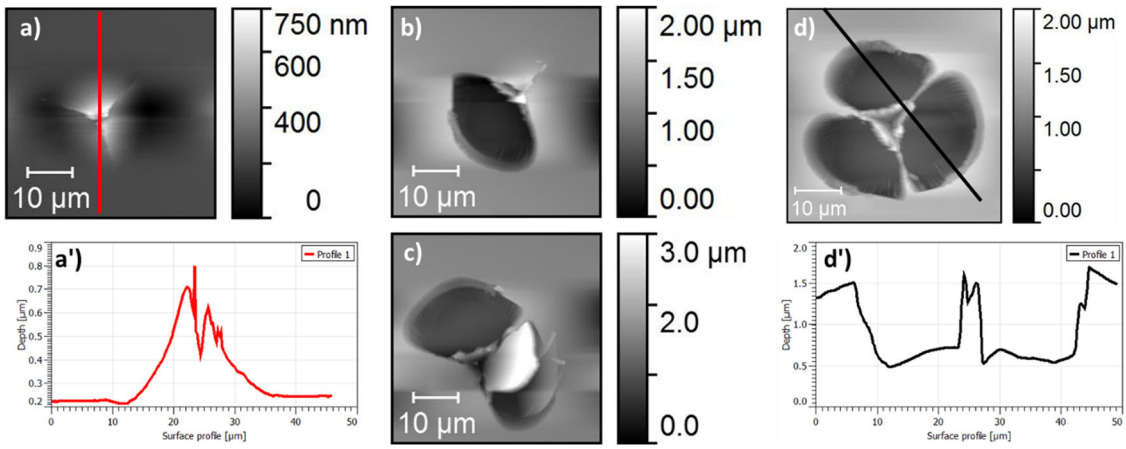

Fig. 12 AFM observations of residual indents in the 1.3 µm thick sol–gel with: **a** no chip, **b** one chip, **c** two chips, and **d** three chips. 2D profiles across residual indents are given in case **a**′ no chipping and **d**′ chipping occurs

sol–gel on glass, a first critical load of about 25–30 mN is found which gives fracture toughness of about 0.1–0.12 MPa.m$^{0.5}$ for the sol–gel and of about 0.7–0.8 MPa.m$^{0.5}$ for the glass substrate. This last result is in agreement with values from CES Selector (0.5–0.8 MPa.m$^{0.5}$) [54], and it confirms that radial cracking may occur in both sol–gel and glass substrate. It is not possible at this stage to indicate which material fails the first during indentation. Level of failure for the different indents is not always the same, and this may originate in local discrepancies of adhesion level (local roughness or interfacial surface contamination) or of the presence of defect in the sol–gel coating. Unfortunately, these result can not be compared with fracture toughness calculated using Eq. 5, given experimental load–displacement curves from this work, which does not present pronounced pop-in. Only smooth slope variations are detected, which does not allow correctly strain energy difference estimation, even-if applying statistical analysis with dedicated Matlab toolbox [72]. Moreover, interfacial fracture toughness can be

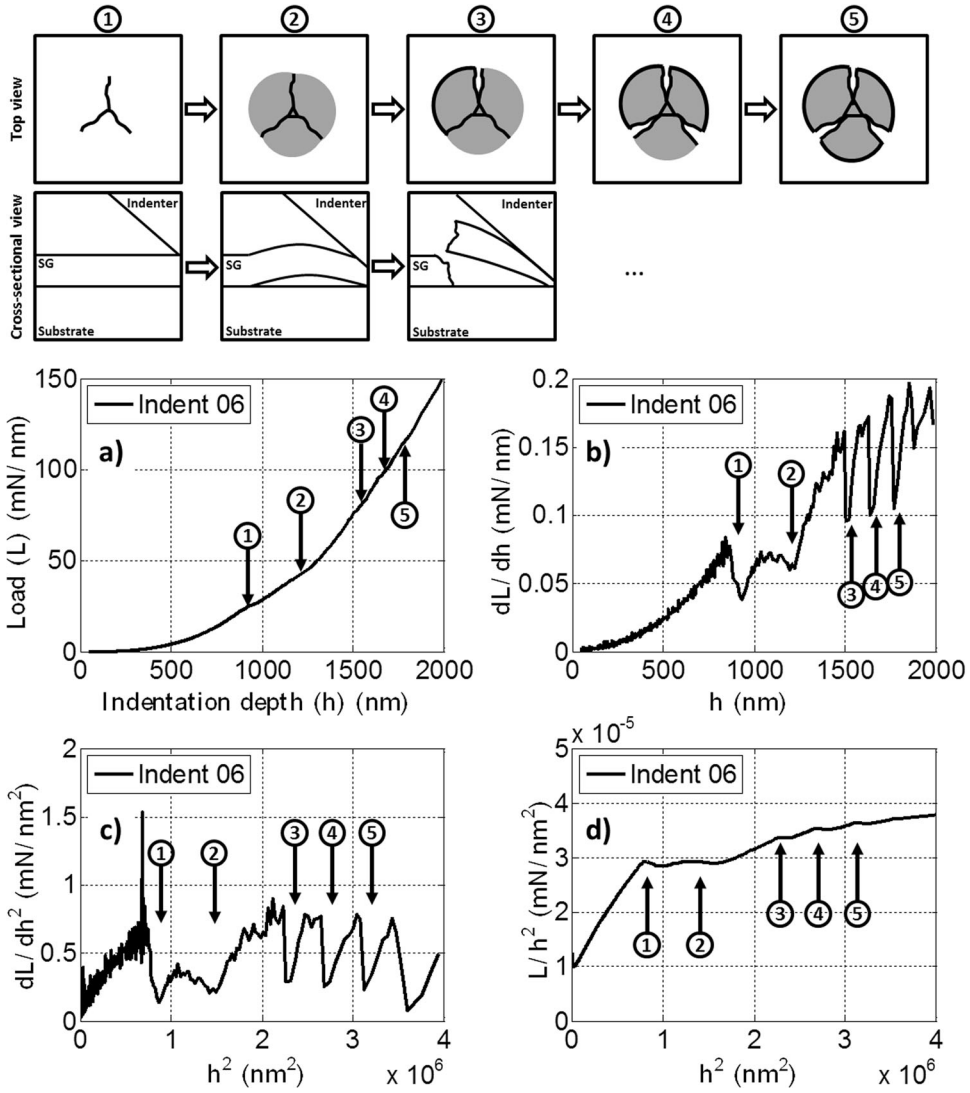

Fig. 13 Evolution of failure mechanisms in the sol–gel coating under indentation: 1 radial cracking, 2 delamination, and 3–5 successive chipping. Different ways to detect failure event: **a** plot of the load (L) vs. displacement (h), **b** plot of dL/dh vs. h, **c** plot of dL/dh^2 vs. h^2, and **d** plot of L/h^2 vs. h^2

estimated from these experiments using respectively Eq. 8 and values are plotted Fig. 16.

3.2.4 Thermal annealing effect

From the scratch experiments, evolution of normalized scratch depth to the coating thickness for sol–gel on glass are plotted Fig. 14, as a function of horizontal indenter displacement, with the corresponding OM observations of the scratch grooves. No major chipping or delamination failure is observed in 275 nm thick sol–gel coatings. For thicker sol–gel coatings, chips are observed along the scratch grooves. Looking at the evolution of the scratch depth, the absolute maximum final depth is much higher when the coating is thicker, as the indenter is not constraint by the substrate. Moreover, slope variations or discontinuities on the mean scratch depth during the penetration of the indenter into the samples are directly correlated to the formation of chips in front of the grooves. Based on this first analysis, it is clear that thermal annealing delays the coating fracture and coating–substrate decohesion. The deformation induced in the annealed sol–gel coating is much more elastic with smaller scratch grooves than the plastic deformation with chipping failure initiation in the nonannealed coating. These results are in agreement with the literature [72] and work of adhesion can be estimated using Eq. 6 and values are reported in Table 4.

3.3 Interfacial fracture estimation

The fracture of the sol–gel coating during nanoindentation and nanoscratch tests is a combination of cohesive and adhesive failure mechanisms. Given that, no network of residual cracks is observed on the different sol–gel coatings (whatever the deposition conditions) (Figs 5 and 8), it is assumed that the residual stress level tends to be very low in

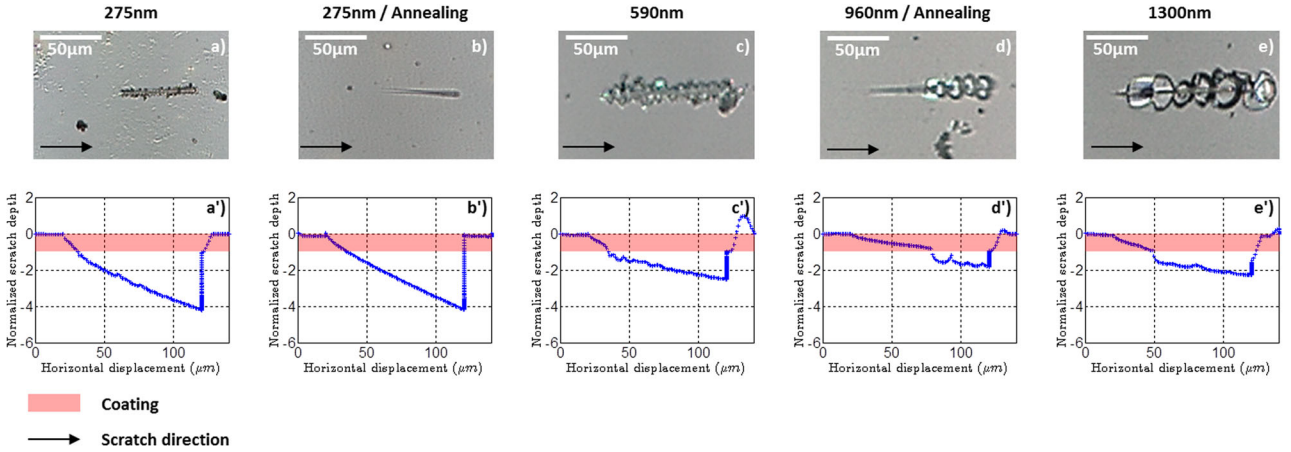

Fig. 14 Evolution of scratch depth as a function of horizontal indenter displacement and the corresponding in situ optical microscopic observations, obtained for only one scratch test on sol–gel deposited on glass substrate

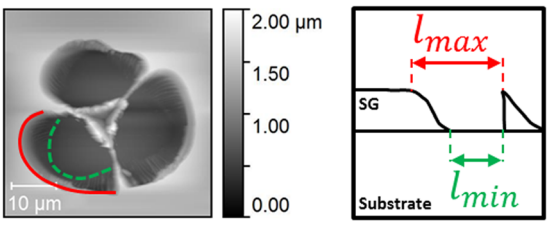

Fig. 15 Definition of the chip lengths to use for interfacial toughness calculation

the studied sol–gel coatings. For that reason, fracture energy dissipated during a chip formation can be estimated using the model from Thouless [50] with Eq. 9 and interfacial fracture are thus estimated using Eqs. 7, 8. Average values for geometrical parameters are assessed from optical micrographs in case of chips formed during indentation and scratch experiments. In case of indentation tests, a more accurate average length ($\bar{l}$) of the chips is defined Eq. 11, as the mean value between the minimum and the maximum lengths measured experimentally (Fig. 15). This average length replaces the geometrical parameter l in Eq. 9. In case of scratch tests, only the first is considered and fracture energy calculations are only done for 590, 960, and 1300 nm thick sol–gel. Elastic modulus and thickness of the sol–gel coatings are taken from Table 3, and a Poisson's ratio for the sol–gel is set to 0.225 [47]. No interfacial fracture is calculated in the case of annealed samples, as no obvious chipping was observed. Interfacial fracture values are reported Fig. 16 and are in the range of 0.02–0. 2 MPa. $m^{0.5}$, which is in agreement with the literature [47]. The same trend for interfacial fracture toughness evolution is observed in both indentation and scratch experiments. Higher is the percentage of NPs incorporated in the sol–gel, higher is the interfacial fracture toughness. The interface might be not stronger in case of steel substrate, but the

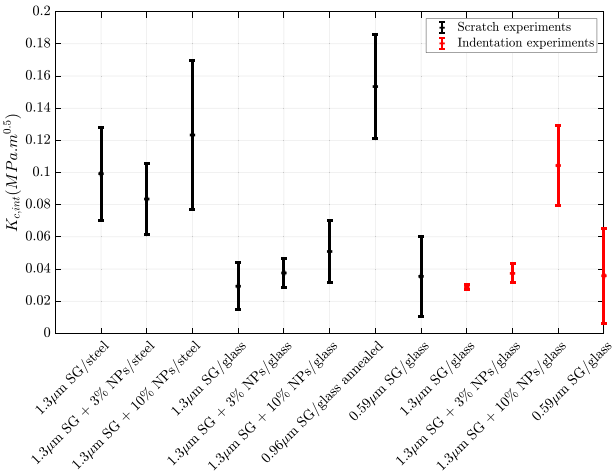

Fig. 16 Evolution of interfacial fracture toughness, calculated with Thouless's model, as a function of substrate, sol–gel thickness, and the presence of NPs

plastic deformation of the steel substrate during the tip penetration might induce less stress into the coating, avoiding too early mechanical failures of the sol–gel. Another interesting remark to emphasize is the high value of interfacial fracture toughness reached in the case of annealed sample. Finally, sol–gel thickness does not sound preponderant on the final mechanical strength of the coating–substrate interface.

$$\bar{l} = \frac{(l_{min} + l_{max})}{2} \tag{11}$$

3.4 Sol–gel coating selection

Following Ashby's methodology based on performance indices [54, 55], and using material and interface properties

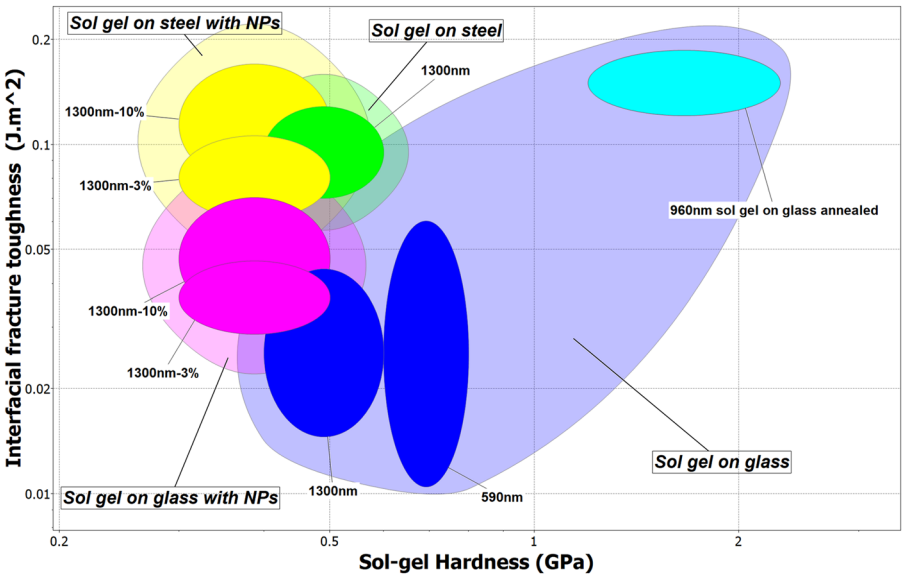

Fig. 17 Ashby map for sol–gel coating selection using CES Selector [54]

obtained experimentally in this work, it is possible to propose the following map to select sol–gel coating for substrate surface protection (Fig. 17). In the *y*-axis, interfacial fracture toughness values are plotted vs. sol–gel hardness values along the *x*-axis for different studied configurations. The hardness property is the performance index use for yielding resistance, in case of a sharp contact with static load. The annealed sol–gel is ideal solution to protect mechanically a glass substrate and a sol–gel with NPs sounds to be the best option for steel surface, as thermal treatment is not possible from an aesthetic point of view (yellowing of the metallic substrate).

4 Conclusion

The mechanical properties and interfacial fracture toughness of sol–gel coatings with different thicknesses and the addition or not of ZrO_2 NPs, deposited on glass and steel substrates were characterized. Nanoindentation was used to extract the elastic modulus and hardness values of the coatings and the substrates. Deep analysis of nanoindentation load–displacement curves leads up to a failure mechanism evolution scenario in the sol–gel coating during indentation. Nanoscratch experiments were performed on the same coating/substrate systems in order to qualify the failure mode of the sol–gel coatings. This work emphasized a strong influence of the thermal treatment (sol–gel three times stiffer and harder), the presence of NPs, and the nature of the substrate on the extraction of mechanical properties of the sol–gel coating and on the failure mechanisms occurring during scratch tests. Based on the nanoindentation and nanoscratch results the estimation of the interfacial fracture toughness is given with values ranging between 0.02 and 0.2 $MPa.m^{0.5}$ for the studied samples and systems. This study shows the interest of the combination of nanoindentation and nanoscratch experiments, for the mechanical characterization of such coatings and sol–gel/substrate interface. Finally, using Ashby method with performance indices, material and interface property map was plotted, which enable an easy and visual sol–gel selection for mechanical protection of steel and glass substrate.

Acknowledgements The authors would like to thank the MecaTech Cluster and the Walloon region for the financial support, in the frame of the Nanosol project. The authors would also like to thank the Walloon region for financial support in the frame of the INDMAT project (BEWARE FELLOWSHIPS), co-funded by the European Union (FP7—Marie Curie Actions). The authors are grateful to Luiza Bonin (UMons) for the 3D microscopic visualization and to Recayi Bilgic (CRM Group) for the AFM observations of residual indents and scratches.

Compliance with ethical standards

Conflict of interest The authors declare that they have no conflict of interest.

Publisher's note Springer Nature remains neutral with regard to jurisdictional claims in published maps and institutional affiliations.

References

1. Aparicio M et al. (2016) Corrosion Protection of AISI 304 Stainless Steel with Melting Gel Coatings. Electrochim Acta 202 (Supplement C):325–332
2. Ćurković L, Ćurković HO, Salopek S, Renjo MM, Šegota S (2013) Enhancement of corrosion protection of AISI 304 stainless steel by nanostructured sol–gel TiO2 films. Corros Sci 77:176–184

3. Feng Z, Liu Y, Thompson GE, Skeldon P (2010) Sol–gel coatings for corrosion protection of 1050 aluminium alloy. Electrochim Acta 55(10):3518–3527
4. Vignesh RB, Edison TNJI, Sethuraman MG (2014) 'Sol–Gel coating with 3-Mercaptopropyltrimethoxysilane as precursor for corrosion protection of aluminium metal. J Mater Sci Technol 30 (8):814–820
5. Nezamdoust S, Seifzadeh D (2017) Application of CeH–V/sol–gel composite coating for corrosion protection of AM60B magnesium alloy. Trans Nonferrous Met Soc China 27 (2):352–362
6. Martini C, Ceschini L (2011) A comparative study of the tribological behaviour of PVD coatings on the Ti-6Al-4V alloy. Tribol Int 44(3):297–308
7. Damasceno JC, Camargo SS, Cremona M (2002) Deposition and evaluation of DLC–Si protective coatings for polycarbonate materials. Thin Solid Films 420–421:195–199
8. Dave BC, Hu X, Devaraj Y, Dhali SK (2004) Sol–gel-derived corrosion-protection coatings. J Sol–Gel Sci Technol 32 (1–3):143–147
9. Wang D, Bierwagen GordonP (2009) Sol–gel coatings on metals for corrosion protection. Prog Org Coat 64(4):327–338
10. Zheng S, Li J (2010) Inorganic–organic sol gel hybrid coatings for corrosion protection of metals. J Sol–Gel Sci Technol 54 (2):174–187
11. Fabes BD, Uhlmann DR (1990) Strengthening of glass by sol-gel coatings. J Am Ceram Soc 73(no. 4):978–988
12. Guglielmi M (1997) Sol-Gel Coatings on Metals. J Sol–Gel Sci Technol 8(1–3):443–449
13. Mammeri F, Le Bouhris E, Rozes L, Sanchez C (2005) Mechanical properties of hybrid organic–inorganic materials. J Mater Chem 15(35–36):3787–3811
14. S Zhang (2010) Nanostructured thin films and coatings: mechanical properties. CRC Press, USA
15. Levy D, Zayat M (2015) The sol–gel handbook: synthesis, characterization and applications, 3–volume set. Wiley VCH, Weinheim
16. Tlili B, Barkaoui A, Walock M (2016) Tribology and wear resistance of the stainless steel. The sol–gel coating impact on the friction and damage. Tribol Int 102:348–354
17. F-X Perrin, 'Films inorganiques et hybrides protecteurs obtenus par voie sol-gel', Techniques de l'ingénieur Traitements de surface des métaux en milieu aqueux. vol. base documentaire: TIB359DUO, no. ref. article: m1722, 2007.
18. Osborne JH et al. (2001) Testing and evaluation of nonchromated coating systems for aerospace applications. Prog Org Coat 41 (4):217–225
19. Yang Y-Q, Liu L, Hu J-M, Zhang J-Q, Cao C-N (2012) Improved barrier performance of metal alkoxide-modified methyltrimethoxysilane films. Thin Solid Films 520(6):2052–2059
20. Rauter A, Slemenik Perše L, Orel B, Bengű B, Sunetci O, Šurca Vuk A (2013) Ex situ IR and Raman spectroscopy as a tool for studying the anticorrosion processes in (3-glycidoxypropyl)trimethoxysilane-based sol–gel coatings. J Electroanal Chem 703:97–107
21. Kunst SR et al. (2014) Corrosion resistance of siloxane–poly (methyl methacrylate) hybrid films modified with acetic acid on tin plate substrates: Influence of tetraethoxysilane addition. Appl Surf Sci 298:1–11
22. Dias SAS, Lamaka SV, Nogueira CA, Diamantino TC, Ferreira MGS (2012) Sol–gel coatings modified with zeolite fillers for active corrosion protection of AA2024. Corros Sci 62:153–162
23. Lamaka SV et al. (2008) Novel hybrid sol–gel coatings for corrosion protection of AZ31B magnesium alloy. Electrochim Acta 53(14):4773–4783
24. Garcia RBR, da Silva FS, Kawachi EY (2013) New sol–gel route for SiO2/ZrO2 film preparation. Colloids Surf A Physicochem Eng Asp 436:484–488
25. Capelossi VR, Poelman M, Recloux I, Hernandez RPB, de Melo HG, Olivier MG (2014) Corrosion protection of clad 2024 aluminum alloy anodized in tartaric-sulfuric acid bath and protected with hybrid sol–gel coating. Electrochim Acta 124:69–79
26. Roussi E, Tsetsekou A, Skarmoutsou A, Charitidis CA, Karantonis A (2013) Anticorrosion and nanomechanical performance of hybrid organo-silicate coatings integrating corrosion inhibitors. Surf Coat Technol 232:131–141
27. Fedel M, Olivier M, Poelman M, Deflorian F, Rossi S, Druart M-E (2009) Corrosion protection properties of silane pre-treated powder coated galvanized steel. Prog Org Coat 66(2):118–128
28. Nicolay A et al. (2015) Elaboration and characterization of a multifunctional silane/ZnO hybrid nanocomposite coating. Appl Surf Sci 327:379–388
29. Sabzi M, Mirabedini SM, Zohuriaan-Mehr J, Atai M (2009) Surface modification of TiO2 nano-particles with silane coupling agent and investigation of its effect on the properties of polyurethane composite coating. Prog Org Coat 65(2):222–228
30. Peng B, Huang Y, Chai L, Li G, Cheng M, Zhang X (2007) Influence of polymer dispersants on dispersion stability of nano-TiO2 aqueous suspension and its application in inner wall latex paint. J Cent South Univ Technol 14(4):490–495
31. Luo K, Zhou S, Wu L (2009) High refractive index and good mechanical property UV-cured hybrid films containing zirconia nanoparticles. Thin Solid Films 517(21):5974–5980
32. Piwoński I, Soliwoda K (2010) The effect of ceramic nanoparticles on tribological properties of alumina sol–gel thin coatings. Ceram Int 36(1):47–54
33. Banerjee DA, Kessman AJ, Cairns DR, Sierros KA (2014) Tribology of silica nanoparticle-reinforced, hydrophobic sol–gel composite coatings. Surf Coat Technol 260:214–219
34. Song J, Liu Y, Liao Z, Wang S, Tyagi R, Liu W (2016) Wear studies on ZrO2-filled PEEK as coating bearing materials for artificial cervical discs of Ti6Al4V. Mater Sci Eng C 69:985–994
35. Atanacio AJ, Latella BA, Barbé CJ, Swain MV (2005) Mechanical properties and adhesion characteristics of hybrid sol–gel thin films. Surf Coat Technol 192(2–3):354–364
36. Fabes BD, Oliver WC (1990) Mechanical properties of sol-gel coatings. J Non-Cryst Solids 121(1):348–356
37. Chan CM, Cao GZ, Fong H, Sarikaya M, Robinson T, Nelson L (2000) Nanoindentation and adhesion of sol-gel-derived hard coatings on polyester. J Mater Res 15(01):148–154
38. Latella BA, Gan BK, Barbé CJ, Cassidy DJ (2008) Nanoindentation hardness, Young's modulus, and creep behavior of organic–inorganic silica-based sol-gel thin films on copper. J Mater Res 23(09):2357–2365
39. J Hay (2009) Mechanical characterization of sol–gel coatings using a nano indenter G200. Application Notes from Agilent Technologies. https://www.agilent.com/
40. Piombini H, Ambard C, Compoint F, Valle K, Belleville PSanchez C (2015) Indentation hardness and scratch tests for thin layers manufactured by sol–gel process. In: CLEO: Applications and Technology
41. Ballarre J, Jimenez-Pique E, Anglada M, Pellice SA, Cavalieri AL (2009) Mechanical characterization of nano-reinforced silica based sol–gel hybrid coatings on AISI 316L stainless steel using nanoindentation techniques. Surf Coat Technol 203 (20–21):3325–3331
42. Malzbender J, de With G, den Toonder JMJ (2000) Determination of the elastic modulus and hardness of sol–gel coatings on glass: influence of indenter geometry. Thin Solid Films 372 (1–2):134–143

43. BA Latella, MV Swain, M Ignat (2012) Indentation and fracture of hybrid sol-gel silica films. In: J Nemecek (ed.) Nanoindentation in materials science, IntechOpen, London (UK)
44. Latella BA, Ignat M (2012) Interface fracture surface energy of sol–gel bonded silicon wafers by three-point bending. J Mater Sci Mater Electron 23(1):8–13
45. Den Toonder JD, Malzbender J, With GD, Balkenende R (2002) Fracture toughness and adhesion energy of sol–gel coatings on glass. J Mater Res 17(01):224–233
46. BA Latella, M Ignat, CJ Barbé, DJ Cassidy, H Li (2004) Cracking and decohesion of sol–gel hybrid coatings on metallic substrates. J Sol–Gel Sci Technol 31(1–3):143–149
47. Malzbender J, Den Toonder JMJ, Balkenende AR, De With G (2002) Measuring mechanical properties of coatings: a methodology applied to nano-particle-filled sol–gel coatings on glass Mater Sci Eng R Rep 36(2):47–103
48. Chen L, Yeap KB, She CM, Liu GR (2011) A computational and experimental investigation of three-dimensional micro-wedge indentation-induced interfacial delamination in a soft-film-on-hard-substrate system. Eng Struct 33(12):3269–3278
49. Mercier D, Mandrillon V, Parry G, Verdier M, Estevez R, Bréchet Y, Maindron T (2017) Investigation of the fracture of very thin amorphous alumina film during spherical nanoindentation. Thin Solid Films 638:34–47. https://doi.org/10.1016/j.tsf.2017.07.040
50. Thouless MD (1998) An analysis of spalling in the microscratch test. Eng Fract Mech 61(1):75–81
51. Malzbender J, de With G (2002) A model to determine the interfacial fracture toughness for chipped coatings. Surf Coat Technol 154(1):21–26
52. Xie Y, Hawthorne HM (2003) Measuring the adhesion of sol–gel derived coatings to a ductile substrate by an indentation-based method. Surf Coat Technol 172(1):42–50
53. Bull SJ, Berasetegui EG (2006) An overview of the potential of quantitative coating adhesion measurement by scratch testing. Tribol Int 39(2):99–114
54. Granta Design Ltd. (2019) CES Selector version 2019, Cambridge (UK). https://grantadesign.com
55. MF Ashby (2011) Materials selection in mechanical design, 4th edn. Butterworth-Heinemann, Oxford (UK)
56. Oliver WC, Pharr GM (1992) An improved technique for determining hardness and elastic modulus using load and displacement sensing indentation experiments. J Mater Res 7 (06):1564–1583
57. Oliver WC, Pharr GM (2004) Measurement of hardness and elastic modulus by instrumented indentation: advances in understanding and refinements to methodology. J Mater Res 19 (1):3–20
58. King RB (1987) Elastic analysis of some punch problems for a layered medium. Int J Solids Struct 23(12):1657–1664
59. Makishima A, Mackenzie JD (1975) Calculation of bulk modulus, shear modulus and Poisson's ratio of glass. J Non-Cryst Solids 17 (2):147–157
60. Ledbetter HM (1981) Stainless-steel elastic constants at low temperatures. J Appl Phys 52(3):1587–1589
61. Fischer-Cripps AC (2011) Nanoindentation, 3rd edn. Springer-Verlag, New York (USA)
62. Mercier D et al. (2010) Mesure de module d'Young d'un film mince à partir de mesures expérimentales de nanoindentation réalisées sur des systèmes multicouches, Matériaux & Techniques 99. https://doi.org/10.1051/mattech/2011029
63. Mercier D (2016) NIMS version 3.2. https://github.com/DavidMercier/NIMS, https://doi.org/10.13140/RG.2.2.13901.03045
64. Lawn BR, Evans AG (1977) A model for crack initiation in elastic/plastic indentation fields. J Mater Sci 12:2195–2199
65. Malzbender J, de With G (2001) The use of the indentation loading curve to detect fracture of coatings. Surf Coat Technol 137(1):72–76
66. Li X, Bhushan B (1998) Measurement of fracture toughness of ultra-thin amorphous carbon films. Thin Solid Films 315 (1):214–221
67. Attar F, Johannesson T (1996) Adhesion evaluation of thin ceramic coatings on tool steel using the scratch testing technique. Surf Coat Technol 78(1–3):87–102
68. Burnett PJ, Rickerby DS (1987) The relationship between hardness and scratch adhesion. Thin Solid Films 154(1–2):403–416
69. Bull SJ, Rickerby DS, Matthews A, Leyland A, Pace AR, Valli J (1988) The use of scratch adhesion testing for the determination of interfacial adhesion: the importance of frictional drag. Surf Coat Technol 36(1):503–517
70. Bull SJ, Rickerby DS (1990) New developments in the modelling of the hardness and scratch adhesion of thin films. Surf Coat Technol 42(2):149–164
71. Bull SJ, Berasetegui EG (2006) An overview of the potential of quantitative coating adhesion measurement by scratch testing. Tribol Int 39(2):99–114
72. Lai C-M, Lin K-M, Rosmaidah S (2012) Effect of annealing temperature on the quality of Al-doped ZnO thin films prepared by sol–gel method. J Sol–Gel Sci Technol 61(1):249–257
73. Bull SJ (1997) Failure mode maps in the thin film scratch adhesion test. Tribol Int 30(7):491–498